Compact gas cell for simultaneous detection of atmospheric aerosol optical properties based on photoacoustic spectroscopy and integrating sphere scattering enhancement

Zhengang Li [a], Jiaxiang Liu [a], Zhiqiang Ning [a,b], Haichun Xu [a,b], Junfang Miao [a,b], Ying Pan [a], Changping Yang [a,b], Yonghua Fang [a,b,*]

[a] *Key Laboratory of Environmental Optics and Technology, Anhui Institute of Optics and Fine Mechanics, Hefei Institutes of Physical Science, Chinese Academy of Sciences, Hefei 230031, China*
[b] *University of Science and Technology of China, Hefei 230026, China*

ARTICLE INFO

ABSTRACT

Atmospheric aerosols play a pivotal role in the earth-atmospheric system. Analyzing their optical properties, specifically absorption and scattering coefficients, is essential for comprehending the impact of aerosols on climate. When different optical properties of aerosols are individually measured using multiple devices, cumulative errors in the detection results inevitably occur. To address this challenge, based on photoacoustic spectroscopy (PAS) and integrating sphere (IS) scattering enhancement, a compact gas cell (PASIS-Cell) was developed. The PASIS-Cell comprises a dual-T-type photoacoustic cell (DTPAC) and an IS. IS is coupled with DTPAC through a transparent quartz tube, thereby enhancing the scattering signal without compromising the acoustic characteristics of DTPAC. Concurrently, DTPAC can realize high-performance photoacoustic detection of absorption signal. Experimental results demonstrate that PASIS-Cell can simultaneously invert atmospheric aerosol absorption and scattering coefficients, with a minimum detection limit of less than 1 Mm^{-1}, showcasing its potential in the analysis of aerosol optical properties.

1. Introduction

Atmospheric aerosols consist of solid or liquid particles suspended in the gaseous medium, typically ranging in size from sub-micrometer to micrometer scale. They encompass both natural components, such as dust, pollen, bacteria, viruses, etc., and anthropogenic emissions like smoke and chemical dust [1,2]. Aerosols can adversely affect human health, contributing to respiratory and cardiovascular diseases [3,4]. Furthermore, analyzing the optical properties of aerosols is crucial for a precise evaluation of their impact on atmospheric radiative forcing and climate dynamics [5,6].

Currently, key methods employed in measuring atmospheric aerosol absorption coefficients encompass filter membrane, differential, and photoacoustic spectroscopy. The filter membrane technique having been established earlier, remains prevalent. Differential techniques, known for their high sensitivity, have garnered considerable attention in recent years [7]. However, the former encounters challenges such as multiple

scattering and optical shadowing. The latter, constrained by limitations related to transmission error and truncation angle (angle of scattering light that cannot be collected), necessitates further enhancements to fulfill measurement criteria for aerosols with weak absorption and strong scattering.

Photoacoustic spectroscopy is a highly sensitive detection technology, highlighting advantages such as high sensitivity, good selectivity, and rapid response [8–13]. This technique finds extensive applications in electric power detection, environmental monitor, combustion analysis, and medical diagnosis [14–19]. The photoacoustic cell, serving as the core of the photoacoustic detection system, significantly influences the performance of photoacoustic detection. In recent years, researchers have designed innovative high-performance photoacoustic cells [20–26], including the Helmholtz photoacoustic cell, differential H-type photoacoustic cell, T-type photoacoustic cell, differential multi-pass photoacoustic cell, and integrating sphere photoacoustic cell. These advancements have notably enhanced the capability of photoacoustic

---

spectroscopy for the detection of trace gases.

In recent research, photoacoustic spectroscopy has emerged as a main method for quantifying aerosol absorption coefficients. This technique offers the distinct advantage of being independent of aerosol scattering properties during in situ detection. The Desert Research Institute in the United States has conducted an extensive study on the wavelength dependence of atmospheric aerosol absorption coefficients using photoacoustic spectroscopy [27]. Similarly, the University of Szeged in Hungary has employed a photoacoustic spectroscopy setup, utilizing a 1064 nm light source and its higher harmonics (266/355/532 nm), to investigate the wavelength dependence of carbonaceous aerosols generated through simulated combustion. This exploration extends to applications like the traceability of urban pollutants [28,29]. At the Michigan Technological University in the United States, researchers conducted measurements of aerosol absorption properties in the visible and near-infrared wavelength bands. Researchers utilized a super-continuum laser as the excitation light source for the photoacoustic spectroscopy device [30,31]. Meanwhile, the Anhui Institute of Optics and Fine Mechanics of the Chinese Academy of Sciences developed both single-wavelength (532 nm) and multi-wavelength (405/532/780 nm) aerosol photoacoustic detection devices. Successfully employing differential photoacoustic spectroscopy, they measured the absorption coefficients of aerosols in the near-infrared wavelength band (1342 nm), overcoming interference from water vapor [32,33]. Subsequently, the institute expanded its efforts by developing an aerosol measurement device based on cavity ring-down and photoacoustic spectroscopy techniques. This advancement allowed for the comprehensive analysis of the absorption and extinction characteristics of atmospheric aerosols [34].

Beyond the absorption coefficient, the scattering coefficient of aerosols emerges as an important parameter in characterizing their optical properties. This parameter is commonly evaluated using integrating nephelometry technology [35]. Integrating nephelometers provide a means to measure the scattering coefficients of aerosols with diverse chemical compositions, playing a significant role in climate impact studies. Ideally, an integrating nephelometer directly quantify the total scattering coefficient of suspended particles, regardless of aerosol size, composition, and physical state. However, practical integrating nephelometers have not yet achieved this ideal state, primarily constrained by factors such as truncation angle, wavelength response, and the non-ideal characteristics of aerosol particle feed.

In aerosol detection applications, the use of different single optical characteristic parameter measurement instruments may result in a lack of uniform measurement standards due to sampling variations and other factors. Consequently, detection results are vulnerable to cumulative errors stemming from sampling losses, changes in aerosol states, variations in cavities, and the detection source (excitation light source). These factors can significantly influence the inversion of aerosol optical characteristic parameters and the analysis of their physical and chemical properties [36,37]. Sharma et al. from Michigan Technological University developed a device proficient in simultaneously detecting aerosol absorption and scattering coefficients. This approach employed both photoacoustic spectroscopy and integrating nephelometry techniques [30]. The device integrated conventional scattering measurement equipment into the buffer of an H-type photoacoustic cell. Additionally, the linear superposition of the H-type photoacoustic cell with the scattering measurement equipment resulted in the destruction of the gas path symmetry inside the photoacoustic cell and an overall increase in the device's size.

This paper introduces a novel compact gas cell, termed PASIS-Cell, which comprises a dual-T-type photoacoustic cell (DTPAC) and an integrating sphere (IS). In this configuration, the IS is coupled with a transparent quartz tube positioned between the two acoustic tubes of the DTPAC. Based on photoacoustic spectroscopy, the DTPAC provides a convenient method for photoacoustic signal detection and frequency correction, effectively reducing background noise arising from the

absorption of light energy by the optical window. The IS acts as an enhanced integrating nephelometer, amplifying the scattering signal and reducing the truncation angle without interfering with the gas path of the DTPAC. It exhibits no adverse effects on the detection of the absorption coefficient. Additionally, the compact mechanical structure of this gas cell contributes to a reduction in the overall size of the detection unit.

2. Theory and design

2.1. Theory of absorption and scattering coefficients detection

2.1.1. Detection of absorption coefficient by photoacoustic spectroscopy

When a modulated light beam illuminates an aerosol sample within a photoacoustic cell, the aerosol particles convert absorbed light energy into thermal energy and cyclically release heat to the surrounding environment, generating a pressure acoustic wave (photoacoustic signal). By recording the photoacoustic signal using a microphone, the aerosol's absorption coefficient can be derived. The amplitude of the photoacoustic signal can be expressed by Eq. (1) [32]:

$$S_{PA} = PMC_{cell}\alpha C \tag{1}$$

where, S_{PA} represents the photoacoustic signal, P denotes the optical power of the modulated light, M stands for the sensitivity of the microphone, C_{cell} signifies the cell constant of the photoacoustic cell, α is the absorption coefficient per unit concentration of the sample (absorption efficiency), C represents the concentration of the sample, and αC represents the absorption coefficient of the measured sample. In practical applications, values for P and M can be obtained through the actual measurement and the technical manual, respectively, while C_{cell} can be deduced from standard gases with known concentrations and absorption coefficients. Consequently, when measuring an aerosol sample, the absorption coefficient αC can be computed using S_{PA}, P, M, and C_{cell}.

2.1.2. Detection of scattering coefficient by integrating nephelometry

When a parallel light beam traverses through a gas cell, it scatters upon encountering aerosol particles within the cell. Positioned above the cell is a photon detector designed to capture scattering photons from aerosol particles intersecting the path of the parallel light. This configuration is commonly referred to as a cell-reciprocal integrating nephelometer (CRIN) [35], as depicted in Fig. 1. Assuming uniform light intensity and aerosol distribution, the total radiation registered by the photon detector results from the cumulative sum of photons scattering at different angles by aerosols situated at various locations along the light path.

The scattering coefficient α_{sca} of aerosols can be expressed as:

$$\alpha_{sca} = 2\pi \int_0^\pi \beta'(\theta)\sin\theta d\theta \tag{2}$$

where $\beta'(\theta)$ is the scattering intensity of the volume microelement at the scattering angle θ. Eq. (2) characterizes the intensity distribution of
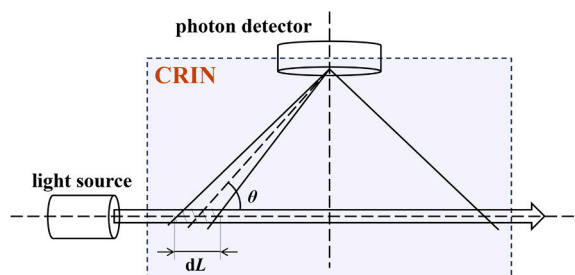

Fig. 1. Schematic diagram of CRIN-based scattering light measurement.

scattering light at various scattering angles. In practical applications, the device can be calibrated using two standard gases with known scattering coefficients [38]. For instance, introducing high-purity (99.9%) CO_2 and particulate-free pure air into the cell allows separate recording of photon counting signals. This data is then utilized to establish the calibration curve relating the scattering coefficient to photon counting signals. Subsequently, the slope (K) and intercept (W) of the calibration curve are calculated. Based on the above, the scattering coefficient of atmospheric aerosols can be determined as:

$$\alpha_{sca} = KC_m - W \tag{3}$$

where, C_m represents the photon counting signal of atmospheric aerosols, K signifies the response relationship between the photon counting signal and the scattering coefficient of the aerosol, and W is the zero offset, indicating the value of the scattering coefficient when the photon counting signal is zero.

2.2. Overall design of a compact gas cell for simultaneous detection

The conventional gas cell for simultaneous detection, based on photoacoustic spectroscopy and integrating nephelometry techniques, adopts a tandem structure [30], as depicted in Fig. 2(a). Positioned on the left side of the gas cell is an H-type photoacoustic cell (HPAC), with a microphone situated in the middle of the acoustic tube to capture the photoacoustic signals emanating from aerosol particles upon absorbing light energy. The buffer on the right side incorporates a CRIN-based integrating nephelometer, employed for detecting the scattering signal. However, the CRIN structure fails to amplify the scattering signal and disrupts the symmetry of the gas path within the HPAC, thereby impeding the achievement of high-precision inversion of the absorption coefficient.

The integrating sphere (IS), functioning as a highly reflective Lambertian body, exhibits superior light mixing properties. When IS employed directly as an integrating nephelometer, a fraction of the scattering photons produced by aerosol particles within the sphere can be collected by the photon detector. Simultaneously, other photons will undergo multiple reflections from the diffuse reflecting material on the inner wall of the sphere. This process stimulates aerosol particles to generate scattering signals anew, thereby enhancing the efficiency of stimulating and collecting scattering light. Nevertheless, this approach has the drawback of contaminating the diffuse reflecting material with aerosols. To address this issue, a quartz tube can be inserted into the IS, as illustrated in Fig. 2(b). When the light beam excites aerosol particles within the quartz tube, scattering signals can be enhanced by leveraging the advantageous characteristics of the IS. This strategy not only

amplifies the scattering signals but also mitigates the risk of contamination of the integrating sphere.

If the CRIN structure depicted in Fig. 2(a) is replaced with the integrating sphere scattering measurement method illustrated in Fig. 2(b), the entire device remains configured in tandem, and the drawback of asymmetry in the air path persists. Capitalizing on the resonance characteristics of the acoustic tubes within the T-type photoacoustic cell (TPAC), where the sound pressure reaches its maximum at the end of the acoustic tubes, a dual-T-type photoacoustic cell (DTPAC) model is devised, as portrayed in Fig. 2(c). In specific resonance modes, the maximum value can be attained at the end of both acoustic tubes. Expanding on this framework, a transparent quartz tube replaces a segment of the absorbing cavity in the middle of the DTPAC. This quartz tube preserves the acoustic properties of the DTPAC while allowing the scattering light to pass through almost losslessly.

In this configuration, IS is coupled with the DTPAC, giving rise to a novel compact gas cell referred to as PASIS-Cell, showcased in Fig. 2(d). This gas cell seamlessly integrates photoacoustic spectroscopy and integrating sphere scattering enhancement technology. The PASIS-Cell not only achieves enhanced photoacoustic and scattering signals but also ensures the symmetry of the gas path within the cell, all while reducing its overall size.

2.3. DTPAC design

2.3.1. Theoretical analysis

The conventional H-type photoacoustic cell, commonly employed for trace gas detection, encounters difficulties in achieving high-sensitivity simultaneous measurements of aerosol absorption and scattering coefficients. To overcome this limitation, a DTPAC model based on the acoustic tube resonance principle was devised, as depicted in Fig. 3. The two acoustic tubes of the DTPAC, in conjunction with the absorption cavity located between them, can be conceptualized as a Tube$_{ACDB}$
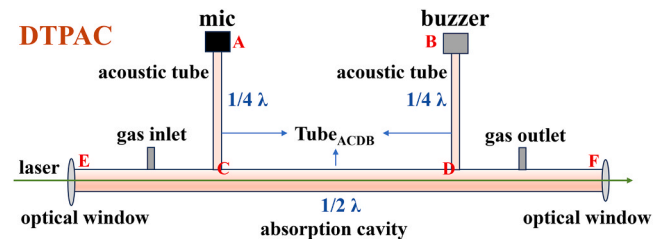
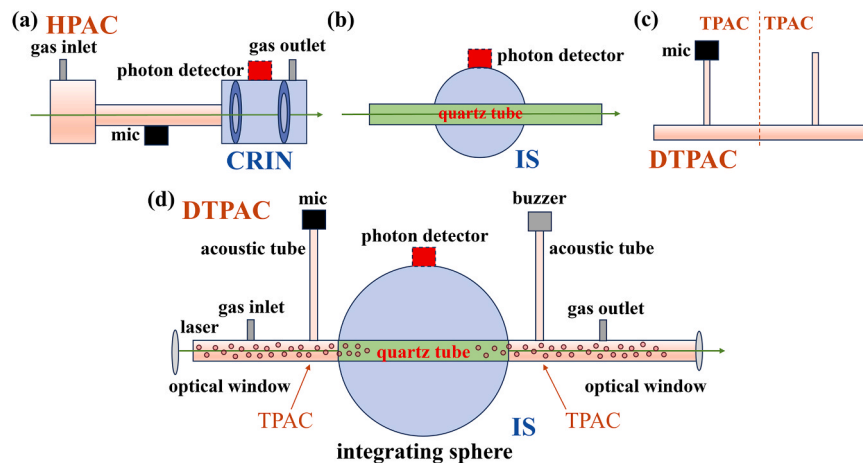**Fig. 3.** Theoretical model of DTPAC.

Fig. 2. Simultaneous detection gas cell design. (a) Simultaneous detection gas cell model with tandem structure; (b) IS scattering measurement model; (c) DTPAC model; (d) PASIS-Cell model.

closed at both ends.

Analyzing the acoustic properties of the two-ended closed acoustic tubes [39], we deduce that when the Tube$_{ACDB}$ is in the second-order resonance mode, three acoustic pressure antinodes (pressure maxima) and two acoustic pressure wave nodes (pressure minima) are generated. The acoustic pressure wave antinodes are situated at the ends of the two acoustic tubes (A, B) and at the midpoint of the absorption cavity. If the length of the acoustic tube (L_{AC}) is $1/4$ λ (acoustic wavelength) and the length of the absorption cavity between the two tubes (L_{CD}) is $1/2$ λ, the acoustic pressure wave nodes are located at the junction of the two acoustic tubes and the absorption cavity (C, D). During this resonance, the acoustic pressure at the end of the acoustic tube is maximal, while the acoustic pressure at the location of the optical windows (E, F) is minimal. This configuration allows the microphone to collect maximal photoacoustic signals, while the window generates low noise.

2.3.2. Simulation and verification

To validate our hypothesis, a resonance mode analysis of the DTPAC with varying acoustic tube lengths was conducted. Utilizing multiphysics field simulation software, a thermo-viscous acoustic simulation model was constructed. The simulation parameters were set to a temperature of 20 ℃ and a pressure of 1 atm inside the photoacoustic cell. The excitation light source for the acoustic pressure wave was a Gaussian light beam with a power density of 0.1 W/kg. The length of the Tube$_{ACDB}$ was divided into four cases ($L_{AC} = 1/4$ L_{CD}; $L_{AC} = 1/2$ L_{CD}; $L_{AC} = L_{EC}$; $L_{AC} = 3/4$ L_{CD}), and Fig. 4 presents the corresponding values along with the simulation results of the photoacoustic cell's resonant modes.

From Fig. 4(a) and (d), it is evident that when L_{AC} is less than or greater than $1/2$ L_{CD}, the acoustic pressure wave nodes shift toward the absorption cavity or inside the acoustic tube, respectively. This shift causes resonance in EC and DF, leading to increased noise at the optical window location. When L_{AC} is equal to L_{EC}, the end of the acoustic tube and the window are almost equivalent for the propagation of the sound wave inside the absorption cavity. Consequently, resonances of close amplitude are generated at both locations, as depicted in Fig. 4(c). When L_{AC} is equal to $1/2$ L_{CD}, the simulation results in Fig. 4(b) demonstrate the desired resonance mode, where the acoustic pressure at the ends of the two acoustic tubes is the largest, and the acoustic pressure at the window location is the smallest. Additionally, there exists a linear relationship between the resonance frequency of the photoacoustic cell and the length of the Tube$_{ACDB}$ for all four cases, exhibiting an R^2 (goodness-of-fit) of 0.997.

Next, the acoustic frequency characteristics of the DTPAC was explored. We simulated the acoustic frequency characteristic curves separately at the end of the acoustic tube and the window location for four different acoustic tube lengths. The outcomes are illustrated in Fig. 5. Notably, when L_{AC} is equal to $1/2$ L_{CD}, the sound pressure at the

end of the acoustic tube reaches a high value, while the sound pressure at the window location is minimized. The ratio of these two sound pressures is approximately 11, significantly surpassing the ratios in the other three cases (1.7, $L_{AC} = 1/4$ L_{CD}; 1.5, $L_{AC} = L_{EC}$; 1.5, $L_{AC} = 3/4$ L_{CD}). Consequently, the signal-to-noise ratio is optimal when L_{AC} is equal to $1/2$ L_{CD}, thus affirming our hypothesis regarding the acoustic properties of the DTPAC.

Based on our investigation of the photoacoustic cell, maintaining a resonance frequency within the range of 1000 to 1500 Hz enables effective suppression of low-frequency noise while preventing the rapid decay of the photoacoustic signal. This insight guides us in establishing the appropriate initial size range for the DTPAC. For a comprehensive exploration of the optimization methodology for the geometric parameters of the photoacoustic cell, readers are referred to our earlier work [18]. The optimized geometric parameters of the DTPAC are presented in Fig. 6(a).

The wide-frequency acoustic characteristic curve of the acoustic tube end, ranging from 500 to 5000 Hz, is obtained through simulation, as illustrated in Fig. 6(b). Notably, the acoustic pressure peaks at the resonance frequency corresponding to the second resonance mode, specifically at 1258 Hz, reaching approximately 5.4×10^{-5} Pa. Under identical simulation conditions, the acoustic pressure amplitude of the DTPAC surpasses that of both the sphere-tube coupled photoacoustic cell (2×10^{-6} Pa) [40] and the H-type differential photoacoustic cell (3×10^{-5} Pa) designed in our previous work [41]. In comparison with recently reported innovative photoacoustic cells, such as the differential integrating sphere photoacoustic cell (1.1×10^{-6} Pa) [25] and the novel T-type photoacoustic cell ($1.2 \sim 6 \times 10^{-5}$ Pa) [23], the DTPAC maintains a competitive edge in terms of acoustic pressure amplitude.

2.3.3. Active correction of resonance frequency

If the photoacoustic cell operates under non-temperature-controlled conditions, the gas sample inside the cell will vary with the ambient temperature, subsequently influencing the resonance frequency of the photoacoustic cell. Fig. 7(a) illustrates the acoustic frequency characteristic curves of the DTPAC at different temperatures. As the temperature increases, the resonance frequency increases, and sound pressure amplitude decreases. To actively address the drift in the resonance frequency, a buzzer at the end of another acoustic tube can be employed to scan near the original resonance frequency. This process enables the retrieval of the latest resonance frequency, and the sound pressure corresponding to the resonance frequency is amplitude-corrected according to the curves presented in Fig. 7(b). This correction compensates for the variations in the photoacoustic signal caused by the drift in the resonance frequency.
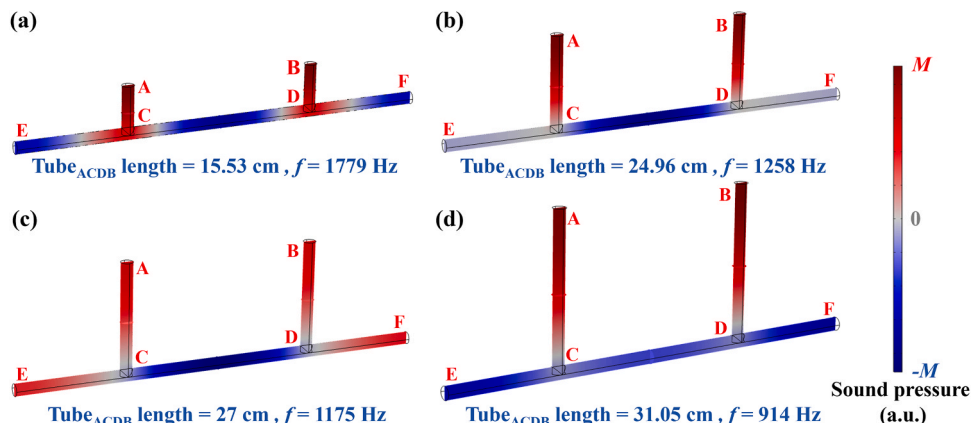

Fig. 4. DTPAC resonance modes for different acoustic tube lengths. (a) $L_{AC} = 1/4$ L_{CD}; (b) $L_{AC} = 1/2$ L_{CD}; (c) $L_{AC} = L_{EC}$; (d) $L_{AC} = 3/4$ L_{CD}.
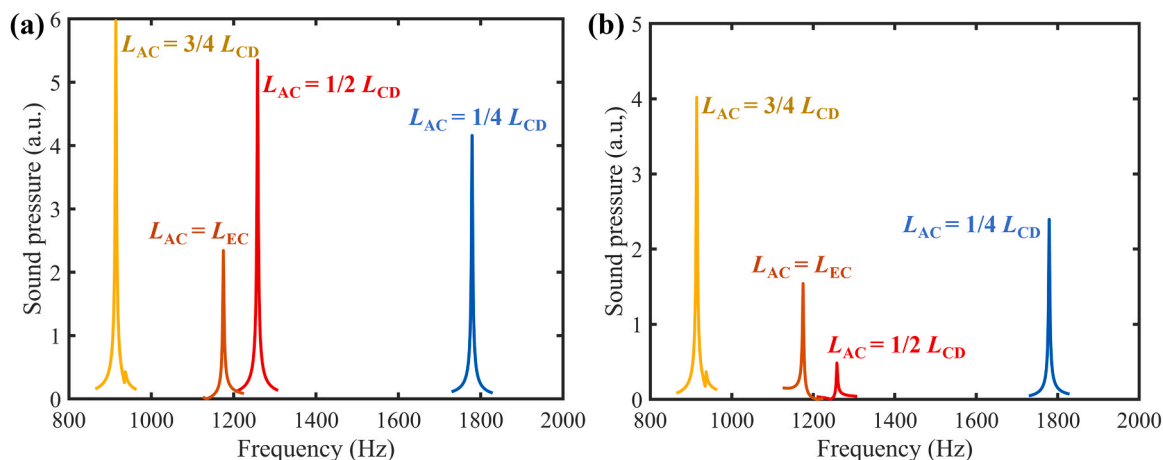
Fig. 5. Acoustic frequency characteristic curves of DTPAC at the end of the acoustic tube and at the window location. (a) End of acoustic tube; (b) Window location.
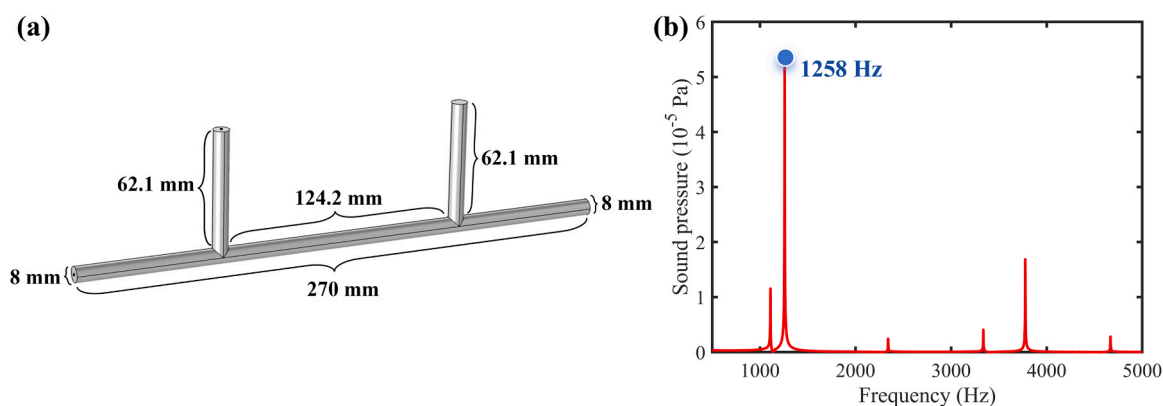

Fig. 6. Simulation of DTPAC wide-frequency acoustic frequency characteristics. (a) Simulation model; (b) Acoustic frequency characteristic curve.
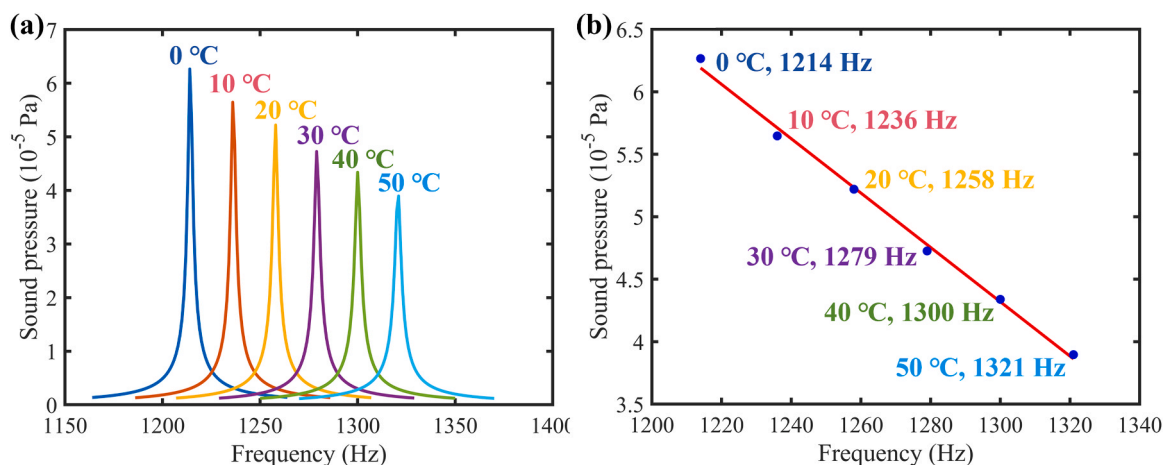

Fig. 7. Simulation of DTPAC acoustic characteristics at different temperatures. (a) Acoustic frequency characteristic curve; (b) Fitted curve of sound pressure amplitude versus resonance frequency.

2.4. IS design

2.4.1. Model construction

If a photon detector is positioned on the inner wall of the absorption cavity between the two acoustic tubes of the DTPAC, it effectively avoids mechanical interference with the microphone, enabling the measurement of the aerosol scattering coefficient. However, the conventional CRIN structure has limited efficiency in collecting scattering light. To

address this, the IS and the DTPAC were integrated, as depicted in Fig. 8 (a). The IS was installed between the two acoustic tubes of the DTPAC, featuring a diffuse reflective material, PTFE (Polytetrafluoroethylene), with an inner wall diameter of 8 cm. The reflectance curve is illustrated in Fig. 8(b), and the reflectance reaches 98.7% near 532 nm. Small holes, each with a 4 mm inner diameter, were strategically positioned on the left and right sides of the integrating sphere, as well as directly above it, to facilitate the mounting of the quartz tube and the photon detector.
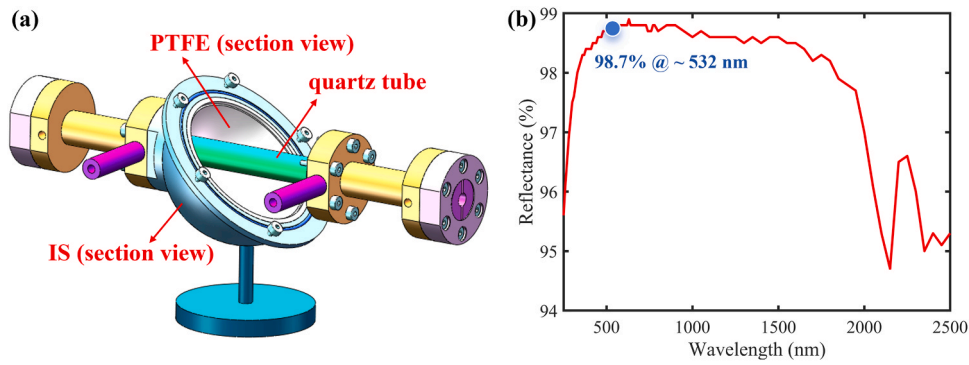
Fig. 8. Coupling model of IS and DTPAC. (a) Mechanical structure. (b) Reflectance curve of the diffuse reflective material PTFE.

The combined opening area of these three holes is significantly less than 5% of the inner surface area of the integrating sphere, rendering the impact on light mixing negligible. Additionally, a high-transmittance quartz tube (96% transmittance @ 532 nm) was employed to minimize the effects of photon absorption and reflection on the scattering coefficient measurement.

2.4.2. Scattering signal detection performance analysis

The absorption cavities on both sides of the DTPAC (EC and DF in Fig. 3) function as the truncation tubes of the integrating sphere nephelometer. The light beam traverses the absorption cavity on the left side of the DTPAC (EC, forward truncation tube), enters the IS through the open aperture, and then exits from the absorption cavity on the right side of the DTPAC (DF, backward truncation tube). To analyze the magnitude of the truncation angle, a mathematical model for the PASIS-Cell scattering measurement was constructed, as depicted in Fig. 9(a). It is assumed that an aerosol particle exists inside the forward truncation tube, and the angle at which its forward scattering light cannot be detected by the photon detector (forward truncation angle) is:

$$\alpha = \tan^{-1}[r/(d_e + d_0)] \tag{4}$$

where r is the radius of the left and right apertures of the integrating sphere, with a value of 4 mm, d_e denotes the distance of an aerosol particle from the aperture of the integrating sphere in the forward truncation tube, with a variation range of $0 \sim 95$ mm, d_0 is the diameter of the sphere. As indicated by Eq. (4), a larger d_0 corresponds to a diminished forward truncation angle. A reduced truncation angle implies a decreased amount of scattering light that cannot be collected, thereby enhancing the precision of the measured scattering coefficient. Without mechanical interference with the DTPAC, a larger size integrating sphere with a diameter of 80 mm was selected. The range of the forward truncation angle calculated as $1.31° \sim 2.86°$, which is smaller than the $7°$ forward truncation angle of the TSI 3563, the commonly used commercial nephelometer. It is evident that the design of a truncation tube significantly reduces the truncation angle [42].

The conventional mathematical model of CRIN scattering measurement is illustrated in Fig. 9(b), which is limited to collecting scattering light generated by an aerosol particle at a specific angle. In contrast, the scattering light produced by an aerosol particle in the integrating sphere is not only directly collected by the photon detector but also benefits from the light-mixing property of the integrating sphere. Part of the scattering light is reflected by the inner wall of the sphere and collected by the photon detector, and another part of the light re-excites the aerosol particles inside the quartz tube to generate scattering signals. Thus, the integrating sphere not only expands the range of scattering light angles that can be collected but also amplifies the intensity of the scattering signal.

2.5. PASIS-Cell design summary

The design of the PASIS-Cell revolves around key considerations such as resonance frequency, resonance modes, sound pressure amplitude, truncation angle, and gas flow characteristics. Initially, by simulating the acoustic properties of the gas cell, the resonance frequency is influenced by the length of the acoustic tube and the separation between the two acoustic tubes. Maintaining a resonance frequency within the range of 1000 to 1500 Hz ensures a larger acoustic signal value while effectively suppressing low-frequency noise. Coupled with the requirement for the acoustic tubes to satisfy $1/4\,\lambda$, the initial size of the DTPAC can be determined.

To achieve a larger truncation angle, a sizable integrating sphere is chosen without introducing mechanical interference. Increasing the length of the truncation tube further diminishes the truncation angle, and it has minimal impact on the acoustic properties of the gas cell. However, this approach complicates gas displacement and enlarges the volume of the detection setup. Additionally, reducing the aperture of the integrating sphere too much is unfavorable for gas flow, and a small aperture complicates the adjustment of the excitation optical path.
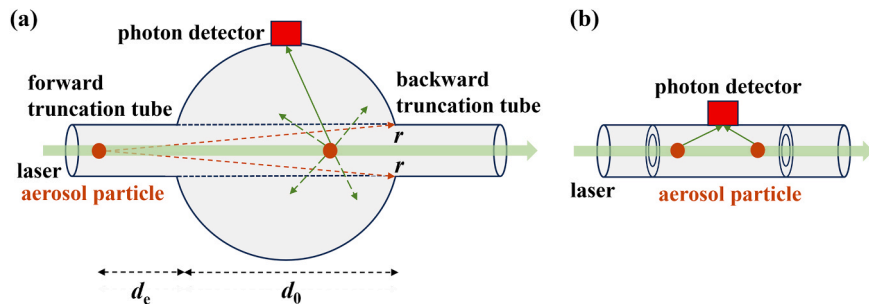

Fig. 9. Scattering signal detection performance analysis. (a) Mathematical model of PASIS-Cell scattering measurement; (b) Mathematical model of conventional CRIN scattering measurement.

3. Experiments and analysis

3.1. Detection setup construction

The structural design of the PASIS-Cell is derived from established models of the DTPAC and IS. Holes are incorporated at the interface between the IS and the photon detector, as well as at the connection to the absorption cavity. The IS housing is constructed from aluminum alloy, and the two hemispheres are securely joined by flanges. The IS is securely connected to the absorption cavity using screws and seals., while the acoustic tubes are sealed with epoxy adhesive where connected to the absorption cavity. The link between the microphone and the end of the acoustic tube is designed with an adjustable diameter flange, allowing for easy replacement of the microphone. The buzzer is embedded at the end of the other acoustic tube. Metal rings secure the optical windows at the light inlet and outlet ports. The 3D mechanical structure of the PASIS-Cell is depicted in Fig. 10(a).

PASIS-Cell served as the central component for constructing a simultaneous detection setup for aerosol absorption and scattering coefficients, as illustrated in Fig. 10(b). The other modules encompass the laser (PGL-V-H-532, CNI), signal generator (AFG3102C, Tektronix), lock-in amplifier (SR865A, SRS), data acquisition card (USB3200N, Art technology), photon detector (H0682, Hamamatsu), photon counter (CH-297, Hamamatsu), microphone (SAC2250, SAC), pump, filter, buzzer, and host computer.

The laser generates a light beam that passes through the PASIS-Cell via an optical window, exciting aerosol particles in the absorption cavity. These aerosol particles then produce the photoacoustic signal. A microphone at the end of the acoustic tube captures the photoacoustic signal, which is subsequently demodulated by a lock-in amplifier. The photon detector, positioned directly above the integrating sphere, collects scattering light from aerosol particles. A pump introduces the measured sample into the gas cell at a constant flow rate of 200 mL/min. To mitigate interference from ambient light, a blackout curtain isolates the detection setup. The absorption cavities on both sides of the PASIS-Cell serve as truncation tubes, further enhancing the scattering signal. The filter adsorbs aerosol particles from the air, creating pure air used for calibrating the scattering coefficient. The host computer communicates with the data acquisition card and the photon counter to invert the absorption and scattering coefficients of the aerosol. To ensure high-precision temperature control and prevent temperature drift from influencing detection results, the detection setup is placed in a temperature-controlled box set at 20 °C.

3.2. Absorption and scattering coefficients calibration

In Section 2.3.2, the theoretical resonance frequency of the photoacoustic cell obtained through simulation is 1258 Hz. However, the actual resonance frequency deviates from the theoretical value due to various factors. Therefore, specific experiments are required to calibrate the actual resonance frequency of the photoacoustic cell. C_2H_2 with a

concentration of 200 ppm was chosen as the measured gas, and a DFB laser (DFB1532 nm, Tengguang) served as the light source. The light source was modulated in the frequency range of 1000 to 1500 Hz. Simultaneously, the photoacoustic signals corresponding to different frequencies were recorded, and the data points underwent Lorentz fitting, as illustrated in Fig. 11(a). The R^2 is calculated to be 0.995, and the resonance frequency of the photoacoustic cell is determined to be 1251 Hz. In comparison with the simulation results, the resonance frequency only exhibits a slight shift of 0.6%.

According to Eq. (1), the absorption coefficient (αC) of the measured aerosol sample can be deduced by calculating the cell constant (C_{cell}) using a standard gas with a known concentration and absorption coefficient. The average value of the photoacoustic signal for 200 ppm C_2H_2 was measured to be 59.5 μV, which can be substituted into Eq. (1) to calculate C_{cell} of about 533 Pa·cm·W^{-1}. To further assess the linearity of the photoacoustic response of the detection setup, relevant experiments were conducted using various concentrations of C_2H_2. The photoacoustic signals generated by different concentrations of C_2H_2 were recorded separately, and the results are depicted in Fig. 11(b), yielding an R^2 of about 0.999. This indicates that the PASIS-Cell exhibits superior photoacoustic response linearity for varying concentrations of gases.

In Section 2.1.2, the calibration method for the scattering coefficient is elucidated. A 532 nm laser diode served as the excitation light source, and high-purity 99.9% CO_2 and pure air, devoid of particulate matter, were utilized as standard gases. The corresponding photon count signals for these two gases were measured, yielding the calibration curve for the scattering coefficients. The values for K and W of the curve were 0.00535 and 99.6, respectively. When analyzing aerosol samples, the scattering coefficients of the aerosols can be determined by referencing the photon count values against the calibration curve. This process enables the assessment of the aerosol's scattering coefficient.

3.3. Detection performance analysis

The photoacoustic detection sensitivity can be calculated by dividing the measured gas concentration value by the signal-to-noise ratio:

$$C_{sensitivity} = C/S_{NR} \tag{5}$$

where C represents the measured gas concentration, and S_{NR} represents the photoacoustic signal-to-noise ratio. When maintaining the laser power (DFB1532 nm, Tengguang) at 8.06 mW, the mean value of the photoacoustic signal generated by 100 ppm C_2H_2 over 100 s was approximately 29.1 μV. Subsequently, pure N_2 was introduced into the photoacoustic cell, and the mean value of the background noise was determined to be 2.5 μV with a standard deviation of 0.1 μV. The S_{NR} was calculated to be 266. Considering the sensitivity of the microphone used to be 50 mV/Pa, the detection sensitivity of the setup for C_2H_2 can be inferred to be 0.38 ppm, with a normalized noise equivalent absorption coefficient of about 3.7×10^{-9} cm^{-1}WHZ$^{-1/2}$.

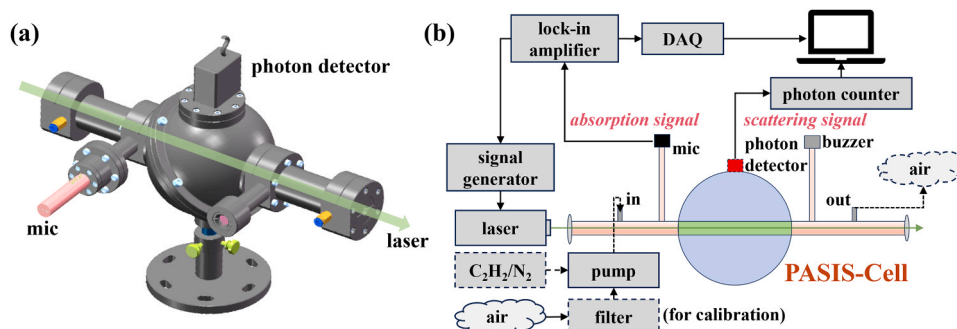The detection limit for the absorption coefficient, denoted as α_{MDL},

Fig. 10. Simultaneous detection setup for aerosol optical properties. (a) 3D mechanical structure of the PASIS-Cell; (b) Schematic diagram of the detection setup.
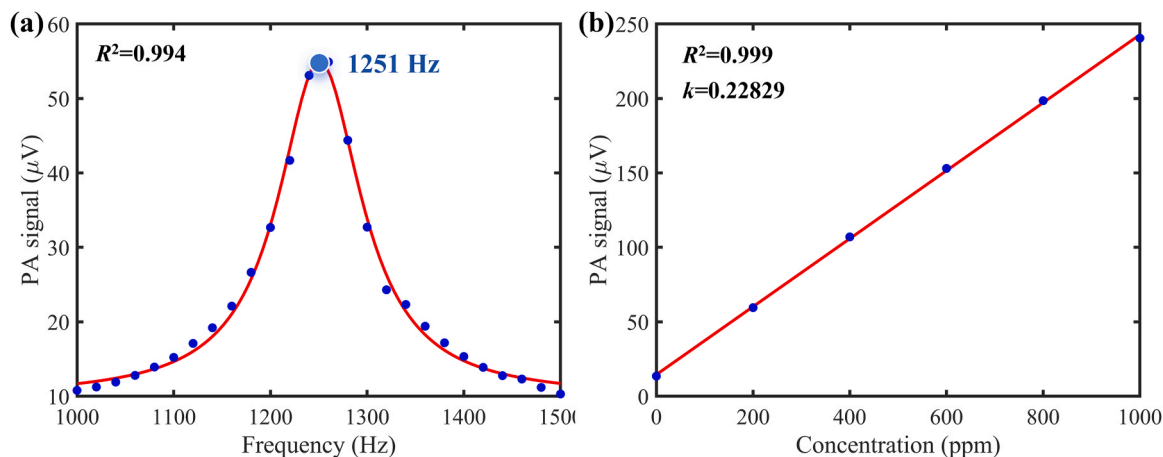
Fig. 11. Acoustic characteristics calibration of detection setup (a) Actual acoustic frequency characteristic curve; (b) Concentration calibration curve.

can be calculated using Eq. (6):

$$\alpha_{MDL} = V_{MDL}/MPC_{cell} \qquad (6)$$

where V_{MDL} represents the limit voltage at which the microphone can detect. The absorption coefficient α_{MDL} was calculated to be approximately 0.95 Mm^{-1}. To establish the detection limit of the scattering coefficient, the scattering coefficient of pure air was measured for 1800 s $\sqrt{2}$ times the average value of the measured scattering coefficient was considered as the minimum detection limit, resulting in about 0.70 Mm^{-1}. This is comparable to the detection limit of commercial integrating nephelometer, underscoring the absorption and scattering coefficient detection capabilities of the PASIS-Cell [43,44].

4. Discussion

4.1. Characterization of aerosol scattering coefficient hygroscopic growth and absorption coefficient daily variation

Aerosol optical properties are influenced by factors such as chemical composition and particle size, closely tied to the relative humidity of the atmosphere. The hydrophilicity of aerosols affects the distribution of particulate matter in the atmosphere, retention time, and the complex refractive index [45,46]. At high relative humidity, the radiative forcing of aerosols is more than twice as high as in dry conditions [44]. To investigate this, relevant experiments were conducted, and the results indicate that the aerosol scattering coefficient in rainy weather is approximately 3 to 4 times that in sunny weather. This observation

confirms the scattering enhancement property of aerosol particles after absorbing moisture. To eliminate the influence of this property, the experiment was conducted one day after five consecutive days of sunny weather. The obtained scattering coefficient of atmospheric aerosols ranged from 47.62 to 199.86 Mm^{-1}, as depicted in Fig. 12(a). In reference [44], the scattering coefficients of atmospheric aerosols were measured using a commercial integrating nephelometer and a self-constructed CRIN device. The measured values fell within the ranges of 59.96 to 187.76 Mm^{-1} and 71.94 to 205.81 Mm^{-1}, respectively, similar to the results presented in this paper.

To assess the capability of the developed setup in analyzing the daily variations of aerosol absorption coefficients, preliminary experiments were conducted at Science Island in Hefei, China. Aerosol absorption coefficients were recorded at four different time periods, as illustrated in Fig. 12(b). The observed variations in absorption coefficients are prominent, primarily attributed to the proximity of the measurement point to a road with motor vehicle exhaust emissions. Notably, 8:40 a.m. corresponds to the peak commuting time, while 18:50 p.m. represents a busy transportation period. The primary contributor to the significant increase in absorption coefficients during these periods is the strongly absorbing black carbon aerosol present in motor vehicle exhaust [43, 46]. Furthermore, the measured atmospheric aerosol absorption coefficients in this study ranged from 59.83 to 149.33 Mm^{-1}, consistent with the results reported in the literature [43]. This consistency further substantiates the potential of the PASIS-Cell for applications in aerosol optical characteristics.
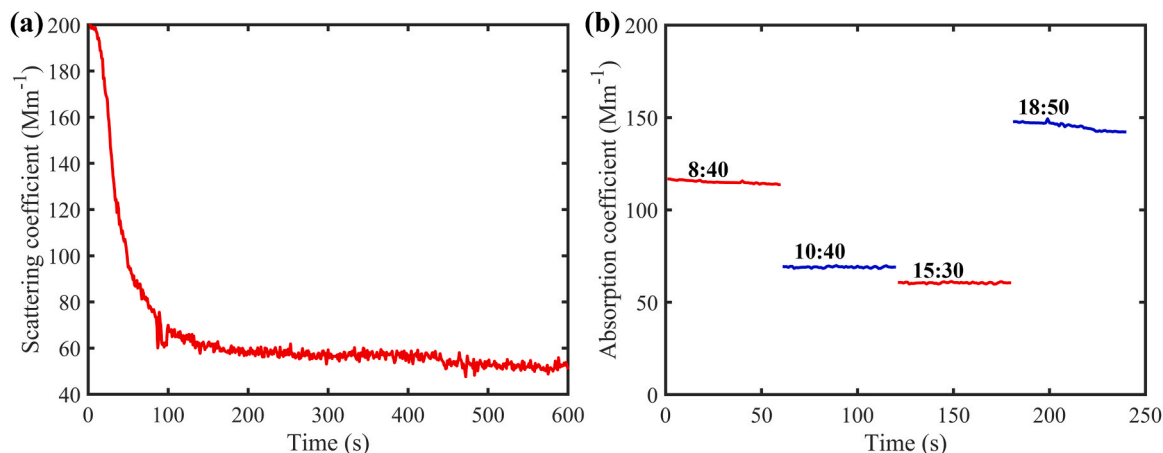

Fig. 12. Optical characteristics analysis of atmospheric aerosols. (a) Scattering coefficient detection result; (b) Absorption coefficient detection result.

4.2. Scattering measurements comparison of PASIS-Cell and DTPAC

To further substantiate the impact of the IS on enhancing the performance of scattering coefficient detection, an equally-sized DTPAC was designed, with the photon detector positioned in the center of the absorption cavity. The experimental findings reveal that the measured scattering coefficients of the DTPAC for aerosol samples deviate from the actual scattering coefficient range, exhibiting high values and poor consistency. This outcome is attributed to the proximity of the photon detector probe to the excitation light beam, inevitably introducing stray light effects that lead to errors and non-repeatability in experimental results. In practical terms, incorporating apertures in the absorption cavity and controlling the distance between the photon detector and the excitation light beam should be considered. However, such measures increase the volume and structural complexity of the cell.

5. Conclusion

In this paper, a compact gas cell named PASIS-Cell was developed. The detailed design process of the gas cell is presented, covering theory, simulation, and performance analysis. Furthermore, we constructed a simultaneous detection setup for measuring aerosol absorption and scattering coefficients. Experimental results demonstrate that the setup achieves a detection limit of 0.95 Mm^{-1} for the absorption coefficient and 0.70 Mm^{-1} for the scattering coefficient, comparable to that of commercial instruments. Additionally, the setup has been employed to analyze the hygroscopic growth of the scattering coefficient and the daily variation characteristics of aerosol absorption coefficients. The experimental findings align closely with results reported in the literature. In our future work, the PASIS-Cell would be further optimized, aiming for precise control of the resonance frequency during field measurements through a temperature control circuit and the buzzer correction method. This optimization will contribute to further reducing the size of the setup. Furthermore, our future endeavors involve conducting large-scale, multi-point aerosol detection and analysis, to achieve three-dimensional monitoring of trace gases and atmospheric aerosols.

CRediT authorship contribution statement

Xu Haichun: Resources, Methodology. **Miao Junfang:** Validation, Supervision. **Ning Zhiqiang:** Software, Methodology, Conceptualization. **Fang Yonghua:** Supervision, Conceptualization. **Pan Ying:** Visualization, Data curation. **Yang Changping:** Visualization, Resources, Project administration. **Li Zhengang:** Writing – original draft, Supervision, Methodology, Investigation, Conceptualization. **Liu Jiaxiang:** Investigation, Funding acquisition.

Declaration of Competing Interest

The authors declare that they have no known competing financial interests or personal relationships that could have appeared to influence the work reported in this paper.

Data Availability

Data will be made available on request.

Acknowledgments

References

[1] A.P. Ault, J.L. Axson, Atmospheric aerosol chemistry: spectroscopic and microscopic advances, Anal. Chem. 89 (1) (2017) 430–452, https://doi.org/10.1021/acs.analchem.6b04670.

[2] T.L. Hoffmann, Environmental implications of acoustic aerosol agglomeration, Ultrasonics 38 (1-8) (2000) 353–357, https://doi.org/10.1016/S0041-624X(99)00184-5.

[3] Z. Peng, J.L. Taylor, J.J. Orlando, G.S. Tyndall, J.L. Jimenez, Organic peroxy radical chemistry in oxidation flow reactors and environmental chambers and their atmospheric relevance, Atmos. Chem. Phys. 19 (2) (2019) 813–834, https://doi.org/10.5194/acp-19-813-2019.

[4] Q. Hong, C. Liu, Q. Hu, C. Xing, W. Tan, H. Liu, Y. Huang, Y. Zhu, J. Zhang, T. Geng, J. Liu, Evolution of the vertical structure of air pollutants during winter heavy pollution episodes: the role of regional transport and potential sources, Atmos. Res. 228 (2019) 206–222, https://doi.org/10.1016/j.atmosres.2019.05.016.

[5] M. Zhang, Y. Ma, W. Gong, B. Liu, Y. Shi, Z. Chen, Aerosol optical properties and radiative effects: assessment of urban aerosols in central China using 10-year observations, Atmos. Environ. 182 (2018) 275–285, https://doi.org/10.1016/j.atmosenv.2018.03.040.

[6] H. Che, B. Qi, H. Zhao, X. Xia, T.F. Eck, P. Goloub, O. Dubovik, V. Estelles, E. C. Agulló, L. Blarel, Y. Wu, J. Zhu, R. Du, Y. Wang, H. Wang, K. Gui, J. Yu, Y. Zheng, T. Sun, Q. Chen, G. Shi, X. Zhang, Aerosol optical properties and direct radiative forcing based on measurements from the China Aerosol Remote Sensing Network (CARSNET) in eastern China, Atmos. Chem. Phys. 18 (1) (2018) 405–425, https://doi.org/10.5194/acp-18-405-2018.

[7] B. Fang, W. Zhao, X. Xu, J. Zhou, X. Ma, S. Wang, W. Zhang, D.S. Venables, W. Chen, Portable broadband cavity-enhanced spectrometer utilizing Kalman filtering: application to real-time, in situ monitoring of glyoxal and nitrogen dioxide, Opt. Express 25 (22) (2017) 26910–26922, https://doi.org/10.1364/OE.25.026910.

[8] C. Zhang, S. Qiao, Y. Ma, Highly sensitive photoacoustic acetylene detection based on differential photoacoustic cell with retro-reflection-cavity, Photoacoustics 30 (2023) 100467, https://doi.org/10.1016/j.pacs.2023.100467.

[9] Z. Li, J. Liu, G. Si, Z. Ning, Y. Fang, Design of a high-sensitivity differential Helmholtz photoacoustic cell and its application in methane detection, Opt. Express 30 (16) (2022) 28984–28996, https://doi.org/10.1364/OE.465161.

[10] Y. Ma, Y. Hong, S. Qiao, Z. Lang, X. Liu, H-shaped acoustic micro-resonator-based quartz-enhanced photoacoustic spectroscopy, Opt. Lett. 47 (3) (2022) 601–604, https://doi.org/10.1364/OL.449822.

[11] F. Wang, J. Wu, Y. Cheng, L. Fu, J. Zhang, Q. Wang, Simultaneous detection of greenhouse gases CH_4 and CO_2 based on a dual differential photoacoustic spectroscopy system, Opt. Express 31 (21) (2023) 33898–33913, https://doi.org/10.1364/OE.503454.

[12] G. Wu, X. Wu, Z. Gong, J. Xing, Y. Fan, J. Ma, W. Peng, Q. Yu, L. Mei, Highly sensitive trace gas detection based on a miniaturized 3D-printed Y-type resonant photoacoustic cell, Opt. Express 31 (21) (2023) 34213–34223, https://doi.org/10.1364/OE.502733.

[13] B. Chen, H. Li, X. Zhao, M. Gao, K. Cheng, X. Shao, H. Wu, L. Dong, X. Yin, Trace photoacoustic SO_2 gas sensor in SF_6 utilizing a 266 nm UV laser and an acousto-optic power stabilizer, Opt. Express 31 (4) (2023) 6974–6981, https://doi.org/10.1364/OE.483240.

[14] P. Zhao, Y. Zhao, H. Bao, H. Ho, W. Jin, S. Fan, S. Gao, Y. Wang, P. Wang, Mode-phase-difference photothermal spectroscopy for gas detection with an anti-resonant hollow-core optical fiber, Nat. Commun. 11 (2020) 847.

[15] F. Wang, Y. Cheng, Q. Xue, Q. Wang, R. Liang, J. Wu, J. Sun, C. Zhu, Q. Li, Techniques to enhance the photoacoustic signal for trace gas sensing: A review, Sens. Actuators A: Phys. 345 (1) (2022) 113807, https://doi.org/10.1016/j.sna.2022.113807.

[16] G.S. Jeng, M.L. Li, M. Kim, S.J. Yoon, J.J. Pitre Jr, D.S. Li, I. Pelivanov, M. O. Donnell, Real-time interleaved spectroscopic photoacoustic and ultrasound (PAUS) scanning with simultaneous fluence compensation and motion correction, Nat. Commun. 12 (1) (2021) 716, https://doi.org/10.1038/s41467-021-20947-5.

[17] I. Pelivanov, E. Petrova, S.J. Yoon, Z. Qian, K. Guye, M.O. Donnel, Molecular fingerprinting of nanoparticles in complex media with non-contact photoacoustics: Beyond the light scattering limit, Sci. Rep. 8 (1) (2018) 14425, https://doi.org/10.1038/s41598-018-32580-2.

[18] Z. Li, J. Liu, G. Si, Z. Ning, Y. Fang, Design of a high-sensitivity differential Helmholtz photoacoustic cell and its application in methane detection, Opt. Express 30 (16) (2022) 28984–28996, https://doi.org/10.1364/OE.465161.

[19] T. Starecki, M.H. Pietrzak, M.K. Ścisłowski, Properties of a symmetrical photoacoustic Helmholtz cell operating with imbalanced counterphase light stimulation, Sensors 23 (16) (2023) 7150, https://doi.org/10.3390/s23167150.

[20] Q. Ma, L. Li, Z. Gao, S. Tian, J. Yu, X. Du, Y. Qiao, C. Shan, Near-infrared sensitive differential Helmholtz-based hydrogen sulfide photoacoustic sensors, Opt. Express 31 (9) (2023) 14851–14861, https://doi.org/10.1364/OE.488835.

[21] X. Yin, M. Gao, R. Miao, L. Zhang, X. Zhang, L. Liu, X. Shao, F.K. Tittel, Near-infrared laser photoacoustic gas sensor for simultaneous detection of CO and H_2S, Opt. Express 29 (21) (2021) 34258–34268, https://doi.org/10.1364/OE.441698.

[22] Z. Gong, T. Gao, L. Mei, K. Chen, Y. Chen, B. Zhang, W. Peng, Q. Yu, Ppb-level detection of methane based on an optimized T-type photoacoustic cell and a NIR diode laser, Photoacoustics 21 (2021) 100216, https://doi.org/10.1016/j.pacs.2020.100216.

[23] L. Zhang, L. Liu, X. Zhang, X. Yin, H. Huan, H. Liu, X. Zhao, Y. Ma, X. Shao, T-type cell mediated photoacoustic spectroscopy for simultaneous detection of multi-

component gases based on triple resonance modality, Photoacoustics 31 (2023) 100492, https://doi.org/10.1016/j.pacs.2023.100492.

[24] X. Zhao, K. Chen, D. Cui, M. Guo, C. Li, H. Qi, G. Zhang, Z. Gong, Z. Zhou, W. Peng, Ultra-high sensitive photoacoustic gas detector based on differential multi-pass cell, Sens. Actuators B: Chem. 368 (2022) 132124, https://doi.org/10.1016/j.snb.2022.132124.

[25] C. Zhang, Y. He, S. Qiao, Y. Ma, Differential integrating sphere-based photoacoustic spectroscopy gas sensing, Opt. Lett. 48 (19) (2023) 5089–5092, https://doi.org/10.1364/OL.500214.

[26] Z. Li, G. Si, Z. Ning, J. Liu, Y. Fang, B. Si, Z. Cheng, C. Yang, Highly sensitive sphere-tube coupled photoacoustic cell suitable for detection of a variety of trace gases: NO_2 as an example, Sensors 22 (1) (2021) 281, https://doi.org/10.3390/s22010281.

[27] M. Gyawali, W.P. Arnott, R.A. Zaveri, C. Song, H. Moosmüller, L. Liu, M. I. Mishchenko, L.W.A. Chen, M.C. Green, J.G. Watson, J.C. Chow, Photoacoustic optical properties at UV, VIS, and near IR wavelengths for laboratory generated and winter time ambient urban aerosols, Atmos. Chem. Phys. 12 (5) (2012) 2587, https://doi.org/10.5194/acp-12-2587-2012.

[28] T. Ajtai, Á. Filep, M. Schnaiter, C. Linke, M. Vragel, Z. Bozóki, G. Szabó, T. Leisner, A novel multi-wavelength photoacoustic spectrometer for the measurement of the UV–vis–NIR spectral absorption coefficient of atmospheric aerosols, J. Aerosol Sci. 41 (11) (2010) 1020–1029, https://doi.org/10.1016/j.jaerosci.2010.07.008.

[29] N. Utry, T. Ajtai, M. Pintér, E. Illés, E. Tombácz, G. Szabó, Z. Bozóki, Generation and UV–VIS–NIR spectral responses of organo-mineral aerosol for modelling soil derived dust, Atmos. Environ. 152 (2017) 553, https://doi.org/10.1016/j.atmosenv.2017.01.012.

[30] N. Sharma, I.J. Arnold, H. Moosmüller, W.P. Arnott, C. Mazzoleni, Photoacoustic and nephelometric spectroscopy of aerosol optical properties with a supercontinuum light source, Atmos. Meas. Tech. 6 (4) (2013) 3501, https://doi.org/10.5194/amt-6-3501-2013.

[31] J.G. Radney, C.D. Zangmeister, Measurement of gas and aerosol phase absorption spectra across the visible and near-IR using supercontinuum photoacoustic spectroscopy, Anal. Chem. 87 (14) (2015) 7356, https://doi.org/10.1021/acs.analchem.5b01541.

[32] Q. Liu, H. Huang, Y. Wang, G. Wang, Z. Cao, K. Liu, W. Chen, X. Gao, Multi-wavelength measurements of aerosol optical absorption coefficients using a photoacoustic spectrometer, Chin. Phys. B 23 (6) (2014) 064205, https://doi.org/10.1088/1674-1056/23/6/064205.

[33] W. Zhu, Q. Liu, Y. Wu, Aerosol absorption measurement at SWIR with water vapor interference using a differential photoacoustic spectrometer, Opt. Express 23 (18) (2015) 23108, https://doi.org/10.1364/OE.23.023108.

[34] H. Jin, R. Hu, P. Xie, P. Luo, Synchronous detection of multiple optical characteristics of atmospheric aerosol by coupled photoacoustic cavity, Chin. Phys. B 31 (6) (2022) 060703, https://doi.org/10.1088/1674-1056/ac43ad.

[35] G.W. Mulholland, N.P. Bryner, Radiometric model of the transmission cell-reciprocal nephelometer, Atmos. Environ. 28 (5) (1994) 873–887, https://doi.org/10.1016/1352-2310(94)90246-1.

[36] W. Zhao, X. Xu, B. Fang, Q. Zhang, X. Qian, S. Wang, P. Liu, W. Zhang, Z. Wang, D. Liu, Y. Huang, D.S. Venables, W. Chen, Development of an incoherent broad-band cavity-enhanced aerosol extinction spectrometer and its application to measurement of aerosol optical hygroscopicity, Appl. Opt. 56 (11) (2017) E16–E22, https://doi.org/10.1364/AO.56.000E16.

[37] S. Singh, M.N. Fiddler, D. Smith, S. Bililign, Error analysis and uncertainty in the determination of aerosol optical properties using cavity ring-down spectroscopy, integrating nephelometry, and the extinction-minus-scattering method, Aerosol Sci. Technol. 48 (12) (2014) 1345–1359, https://doi.org/10.1080/02786826.2014.984062.

[38] T.L. Anderson, D.S. Covert, S.F. Marshall, M.L. Laucks, R.J. Charlson, A. P. Waggoner, J.A. Ogren, R. Caldow, R.L. Holm, F.R. Quant, G.J. Sem, A. Wiedensohler, N.A. Ahlquist, T.S. Bates, Performance characteristics of a high-sensitivity, three-wavelength, total scatter/backscatter nephelometer, J. Atmos. Ocean. Technol. 13 (5) (1996) 967–986, https://doi.org/10.1175/1520-0426(1996)013<0967:PCOAHS>2.0.CO;2.

[39] A. Miklós, P. Hess, Z. Bozóki, Application of acoustic resonators in photoacoustic trace gas analysis and metrology, Rev. Sci. Instrum. 72 (4) (2001) 1937–1955, https://doi.org/10.1063/1.1353198.

[40] Z. Zhi, Z. Li, J. Liu, Y. Fang, Methane and carbon dioxide mixed gas detection based on sphere-tube coupled photoacoustic cell, Opt. Commun. 527 (2023) 128977, https://doi.org/10.1016/j.optcom.2022.128977.

[41] Z. Li, J. Liu, G. Si, Z. Ning, Y. Fang, Y. Pan, Optimization design of H-type differential photoacoustic cell and NO_2 detection, Acta Opt. Sin. 42 (18) (2022) 234–243, https://doi.org/10.3788/AOS202242.1830004.

[42] W. Zhao, X. Xu, M. Dong, W. Chen, X. Gu, C. Hu, Y. Huang, X. Gao, W. Huang, W. Zhang, Development of a cavity-enhanced aerosol albedometer, Atmos. Meas. Tech. 7 (8) (2014) 2551–2566, https://doi.org/10.5194/amt-7-2551-2014.

[43] H. Jin, R. Hu, P. Xie, C. Huang, F. Wang, C. Liu, Study on the photoacoustic technology to simultaneous in-situ detection of the cavity ring-down spectrum for multi-optical parameters, IEEE Photonics J. 12 (2) (2020) 1–11, https://doi.org/10.1109/JPHOT.2020.2969226.

[44] Y. Hong, X. Che, H. Su, Z. Mai, Z. Huang, W. Huang, W. Chen, S. Liu, W. Gao, Z. Zhou, G. Tan, X. Li, Exhaled breath analysis using on-line preconcentration mass spectrometry for gastric cancer diagnosis, J. Mass Spectrom. 56 (4) (2021) e4588, https://doi.org/10.1002/jms.4588.

[45] U. Lohmann, J. Feichter, Global indirect aerosol effects: a review, Atmos. Chem. Phys. 5 (3) (2005) 715–737, https://doi.org/10.5194/acp-5-715-2005.

[46] F. Chen, W. Xu, L. Wang, Research on optical absorption characteristics of Ag nanoparticles, Mod. Phys. Lett. B 27 (11) (2013) 1350079, https://doi.org/10.1142/S0217984913500796.
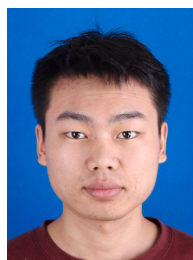
Zhengang Li received his Ph.D. degree from University of Science and Technology of China in 2023. He is now a Postdoctor at Hefei Institutes of Physical Sciences, Chinese Academy of Sciences. His research interests include applications of photoacoustic spectroscopy in the field of trace gas and aerosol detection.

Jiaxiang Liu received his Ph.D. degree from University of Chinese Academy of Sciences, China, in 2015. He is now an associate research fellow at Hefei Institutes of Physical Sciences, Chinese Academy of Sciences. His research interests include applications of infrared spectroscopy in the analysis of trace samples in the field.

Zhiqiang Ning received his M.S. degree in environmental engineering from University of Science and Technology of China, China, in 2020. He is now pursuing a PhD degree of pattern recognition from University of Science and Technology of China. His research interests include infrared hyperspectral imaging information processing.

Haichun Xu received his B.S. degree from Anhui University of Technology, China, in 2019. He is now pursuing a PhD degree of precision instrumentation and machinery from University of Science and Technology of China. His research interests include high-performance sound pressure sensors research for photoacoustic detection.
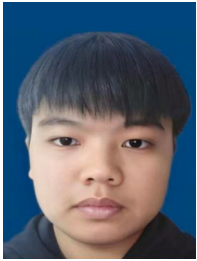
Junfang Miao received his B.S. degree in Measurement Control Technology and Instrumentation from Yantai University, China, in 2020. He is currently pursuing a Ph.D. degree in Physics at the University of Science and Technology of China. His research interests include the application of photoacoustic and Raman spectroscopy in the field of trace gas detection.

Changping Yang received his B.S. degree in software engineering from East China University of Technology in 2019. He is now pursuing for a M.S. degree in resources and environment from the School of Environmental Science and Optoelectronic Technology, University of Science and Technology of China. His research interest is the technology of aerosol monitoring.

Ying Pan received her B.S. degree at Anhui University in 2012. She is now working as an assistant engineer at Hefei Institutes of Physical Sciences, Chinese Academy of Sciences. Her research interests include applications of environmental engineering.

Yonghua Fang graduated from Nanjing University of Aeronautics and Astronautics in 1986, and received his M.S. and Ph. D. degree in Anhui Institute of Optics & Fine Mechanics, Chinese Academy of Sciences (CAS), in 1992 and 1998, respectively. From1986 to1998, he worked at Anhui Institute of Optics & Fine Mechanics as an assistant professor in 1992, associate professor in 1998. During 1998–2000, he was a postdoctoral fellow in Changchun Institute of Optics, Fine Mechanics and Physics, CAS. From 2000 to 2002, he worked at Max Planck Institute for Meteorology, Germany, as a visiting scientist. Since 2002, he has been a processor at Anhui Institute of Optics & Fine Mechanics, CAS. His research interests include remotely sensed information characterization and optoelectronic information detection.